

# PHOTONICS Research

## Edge enhancement through scattering media enabled by optical wavefront shaping

ZIHAO LI,<sup>1,2,5,†</sup>  ZHIPENG YU,<sup>1,2,†</sup>  HUI HUI,<sup>3,†</sup>  HUANHAO LI,<sup>1,2</sup>  TIANING ZHONG,<sup>1,2</sup>  
HONGLIN LIU,<sup>4</sup>  AND PUXIANG LAI<sup>1,2,\*</sup> 

<sup>1</sup>Department of Biomedical Engineering, The Hong Kong Polytechnic University, Hong Kong SAR, China

<sup>2</sup>The Hong Kong Polytechnic University Shenzhen Research Institute, Shenzhen 518000, China

<sup>3</sup>CAS Key Laboratory of Molecular Imaging, Institute of Automation, Chinese Academy of Sciences, Beijing 100190, China

<sup>4</sup>Key Laboratory for Quantum Optics, Shanghai Institute of Optics and Fine Mechanics, Chinese Academy of Sciences, Shanghai 201800, China

<sup>5</sup>Currently at: Department of Bioengineering, University of Pennsylvania, Philadelphia, Pennsylvania 19104, USA

\*Corresponding author: [puxiang.lai@polyu.edu.hk](mailto:puxiang.lai@polyu.edu.hk)

Received 13 January 2020; revised 10 March 2020; accepted 5 April 2020; posted 6 April 2020 (Doc. ID 388062); published 28 May 2020

Edge enhancement is a fundamental and important topic in imaging and image processing, as perception of edge is one of the keys to identify and comprehend the contents of an image. Edge enhancement can be performed in many ways, through hardware or computation. Existing methods, however, have been limited in free space or clear media for optical applications; in scattering media such as biological tissue, light is multiple scattered, and information is scrambled to a form of seemingly random speckles. Although desired, it is challenging to accomplish edge enhancement in the presence of multiple scattering. In this work, we introduce an implementation of optical wavefront shaping to achieve efficient edge enhancement through scattering media by a two-step operation. The first step is to acquire a hologram after the scattering medium, where information of the edge region is accurately encoded, while that of the nonedge region is intentionally encoded with inadequate accuracy. The second step is to decode the edge information by time-reversing the scattered light. The capability is demonstrated experimentally, and, further, the performance, as measured by the edge enhancement index (EI) and enhancement-to-noise ratio (ENR), can be controlled easily through tuning the beam ratio. EI and ENR can be reinforced by  $\sim 8.5$  and  $\sim 263$  folds, respectively. To the best of our knowledge, this is the first demonstration that edge information of a spatial pattern can be extracted through strong turbidity, which can potentially enrich the comprehension of actual images obtained from a complex environment. © 2020 Chinese Laser Press

<https://doi.org/10.1364/PRJ.388062>

### 1. INTRODUCTION

Edge enhancement is uniquely important as perception of edge is a key factor for the human visual system to identify or comprehend the contents of an image. It has vital roles in broad applications, such as increasing discrimination capacity in pattern recognition [1], detecting dislocation of crystal in biological cells [2], and identifying lesion boundaries of cancer [3–6]. The realization of edge enhancement can be traced back to Zernike's seminal work [7], where the phase or intensity gradient of an object is enhanced for conspicuity strengthening and tiny-feature detection. Nowadays, edge enhancement can be accomplished digitally through signal processing methods, such as spatial differentiation [8], wavelet transform [9], and Hilbert transform [10], or through physical settings. One well-known example is spiral phase contrast (SPC) imaging, where a spiral phase plate with a topological charge  $l = 1$  is placed in the Fourier plane of a  $4f$  system [11–13]. Due to the peculiar symmetry of spiral phase, gradients of the phase and

intensity profile can be isotropically enhanced. The SPC method was later extended for microscopy to make image brightness and contrast significantly better than conventional versions [14]. Another strategy is to employ the photorefractive effect to highlight the edge information of an intensity pattern [15–17]. Responding to the interferogram, photorefractive materials, governed by the four-wave-mixing mechanism [15], form a volumetric optical grating with different local diffraction efficiencies. Manipulating such gratings may maximize the diffraction efficiency for edges only while minimizing that for other parts; consequentially, the boundaries of the pattern are enhanced [15]. In addition, some physical filters, such as the Laguerre–Gaussian spatial filter [18] and Airy spiral phase filter [19], are also developed to achieve high contrast edge enhancement.

While promising, all filters mentioned above, no matter digital or physical, can only perform edge detection in free space or process signals obtained with ballistic or quasi-ballistic light.

These approaches are not able or have not been verified to be compatible with strong scattering media (e.g.,  $\sim 1$  mm beneath human skin [20]), when photons are multiply scattered and optical information is completely disordered [21]. Therefore, existing edge enhancement methods encounter the same trade-off between penetration depth and resolution as all other biomedical optical techniques [22]. High-resolution edge information processing and retrieval at depths in scattering media have been desired in many optical applications that yet remain unexplored.

This study aims to tackle this challenge from the perspective of optical wavefront shaping, a relatively new field conceived to manipulate scattered light beyond the diffusion limit [23–27]. Optical phase conjugation (OPC) [24,27–29] is an example of wavefront shaping that exploits the bilateral nature of a light trajectory to “time-reverse” scattered light [30]. The execution of OPC requires an analog [27,31] or digital [28,29,32,33] phase conjugation mirror (PCM) that, first, holographically records the phase profile of scattered light and, second, projects its phase-conjugated copy back to the medium. As a result, the intensity profile of the original incident light field before being scattered can be reconstructed. The whole procedure can be accomplished with two or three steps [33], achieving light manipulation through turbidity as rapidly as a few milliseconds [34,35]. While related, such a capability thus far has not yet been extended for edge enhancement through scattering media. In this study, we take inspiration from the classic photorefractive approach for edge enhancement in free space [15], and develop a digital optical phase conjugation (DOPC) setup to achieve robust and tunable time-reversed speckle suppression and edge enhancement through thick scattering media by a two-step procedure. First, a hologram that accurately encodes the information of the edge only is recorded. Second, the edge pattern is selectively decoded by phase conjugating the scattered light. The proposed method is demonstrated experimentally with scalable edge enhancement performance out of seemingly random speckle patterns. Although a lot needs to

be furthered, this work potentially can be of instructive significance to the processing, comprehension, and analysis of optical images with the presence of scattering.

## 2. METHODS

### A. Experimental Setup

The configuration of the DOPC system is presented in Fig. 1. A CW laser source (EXLSR-532-200-CDRH, Spectra Physics, coherence length = 300 m) emits a laser beam ( $\lambda = 532$  nm), which is split by a beam splitter cube ( $BS_1$ ) into two arms. One is probe beam, and the other is multifunctional beam (calibration/reference/playback beam). The probe beam is expanded by a collimated beam expander, and its intensity profile is shaped by a 1951 USAF resolution test chart (Edmund Optics Inc.). The image of the resolution test chart is relayed onto the interior surface of a diffuser (600 grit polished, Thorlabs) by  $L_6$ . On the other side, the multifunctional beam is spatially shaped by a single-mode fiber (HP-532, Thorlabs, 1 m long) to mimic a quasi-ideal point source at the exit of the collimator ( $C_2$ ). The beam is expanded by a best-form lens ( $L_1$ ) before entering the digital PCM module. At the beam splitter cube ( $BS_4$ ), the probe beam and the multipurpose beam merge and are relayed together to the digital PCM, which is configured by the combination of a scientific complementary metal–oxide semiconductor camera (sCMOS; pco.edge 5.5; PCO; pixel size,  $6.5 \mu\text{m} \times 6.5 \mu\text{m}$ ) and a phase-only spatial light modulator (SLM, PLUTO-VIS-056, HOLOEYE). The SLM and the sCMOS camera are pixel-to-pixel conjugated to each other, with a misalignment error less than 1 pixel. The diffused light pattern right after the diffuser is imaged on the plane of SLM through a  $4f$  system configured by  $L_2$  and  $L_3$ , where the diffuser and the plane of SLM are spatially quasi-conjugated with each other. The digital PCM has two main purposes, hologram recording and playback, which are, respectively, accomplished by the sCMOS camera and the phase-only SLM. To observe the playback wavefront, another CMOS camera (Cam<sub>2</sub>; pixel size,  $2.5 \mu\text{m} \times 2.5 \mu\text{m}$ ) and  $L_5$  are employed to image the reconstructed intensity

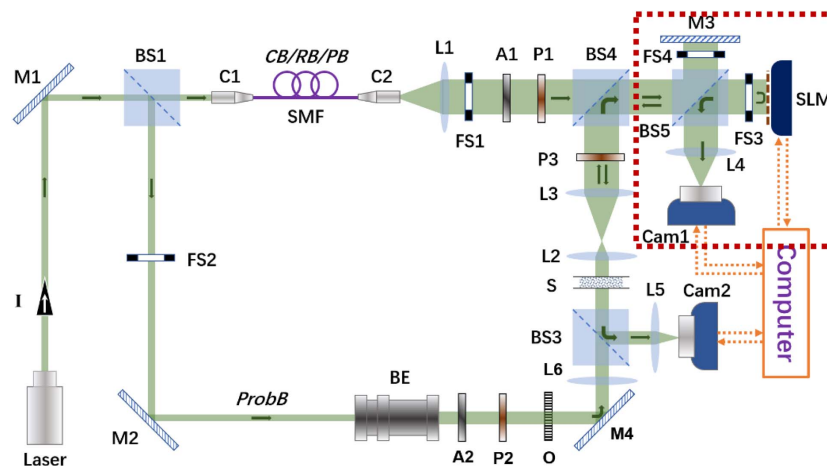


**Fig. 1.** System setup of DOPC.  $A_{1-2}$ , neutral-density attenuator; BE, collimated beam expander;  $BS_{1-5}$ , beam splitter cube;  $C_{1-2}$ , optical fiber collimator; Cam<sub>1</sub>, scientific complementary metal–oxide semiconductor (sCMOS) camera; Cam<sub>2</sub>, CMOS camera;  $FS_{1-4}$ , fast shutter; I, Isolator;  $L_{1-3,5,6}$ , best-form lens;  $L_4$ , camera lens; Laser, CW laser,  $\lambda = 532$  nm;  $M_{1-4}$ , mirror; O, object, a 1951 USAF resolution test chart;  $P_{1-3}$ , linear polarizer; S, scattering medium; SLM, phase-only spatial light modulator; SMF, single-mode optical fiber; CB/RB/PB, calibration/reference/playback beam; ProbB, Probe beam. Red dashed line indicates the module of digital phase conjugation mirror (PCM).

distribution of the playback beam after transmitting through the turbid sample. Polarizations and intensities of the probe beam and the multipurpose beam are adjusted by two linear polarizers ( $P_1$  and  $P_2$ ) and neutral-density attenuators ( $A_1$  and  $A_2$ ), respectively. Four fast shutters ( $FS_{1-4}$ ) are equipped to control the ON or OFF state of light beams. Detailed procedures of the DOPC operation can be referred to Refs. [32,33].

## B. Principles of DOPC-Based Edge Enhancement through Scattering Media

A former study has demonstrated how edges of a binary pattern can be enhanced in free space via the photorefractive effect with a piece of BaTiO<sub>3</sub> photorefractive crystal [15]. The method proposed in this work is actually a digital analogue of the aforementioned photorefractive edge enhancer. Functions of the photorefractive crystal are provided by a digital PCM, a spatially conjugated camera-SLM module, as enclosed by the red dashed line in Fig. 1. On one hand, holographic information is recorded digitally using a digital camera (Cam<sub>1</sub>, Fig. 1); on the other hand, an SLM is able to create variable phase profiles, mimicking the effect of grating with variable diffraction efficiency in the crystal.

Starting with hologram recording, the working principles of DOPC-based edge enhancement can be explained as below. The hologram recorded by Cam<sub>1</sub> can be written as

$$I_h = I_{\text{ref}} + I_{\text{prob}} + 2 \cos \varphi \sqrt{I_{\text{ref}} \cdot I_{\text{prob}}}, \quad (1)$$

where  $I_h$ ,  $I_{\text{ref}}$ , and  $I_{\text{prob}}$  denote the intensity of hologram, the reference beam, and the probe beam, respectively;  $\varphi$  is the phase difference between the reference beam and the probe beam. The local modulation efficiency (M.E.) of PCM, determined by contrast of the hologram recorded by Cam<sub>1</sub>, can be expressed as

$$\text{M.E.} = \frac{I_h}{I_{\text{ref}} + I_{\text{prob}}} = 1 + \text{MD} \cdot \cos \varphi. \quad (2)$$

It can be seen that the local M.E. of PCM is dominated by the modulation depth ( $\text{MD} = \frac{2\sqrt{I_{\text{prob}} \cdot I_{\text{ref}}}}{I_{\text{prob}} + I_{\text{ref}}}$ ) [15]. This term can be expressed as a function of the intensity ratio of the probe and reference beams, i.e.,  $r = \frac{I_{\text{prob}}}{I_{\text{ref}}}$ , so that  $\text{MD}(r) = \frac{2\sqrt{r}}{1+r}$ . As a result, M.E. can be written as  $\text{M.E.} = 1 + \text{MD}(r) \cdot \cos \varphi$ . Considering the one-dimensional situation as follows without scattering media:

$$I_{\text{ref}}(x) = a(\text{for all } x); I_{\text{prob}}(x) = \begin{cases} 0 & x \leq -m/2 \\ b & -m/2 < x < m/2, \\ 0 & x \geq m/2 \end{cases} \quad (3)$$

where  $a$ ,  $b$ , and  $m$  are three finite constants. It represents a simple case of a hologram written to Cam<sub>1</sub>, where the reference beam is of uniform intensity while the probe beam is of a binary intensity profile, i.e., a box function with a width of  $m$ , symmetrical with respect to the origin. But, there is an extreme condition for this situation, that is the intensity of the probe beam is considerably larger than that of the reference beam, i.e.,  $a \ll b$ . For the dark region of the probe beam

( $x < -\frac{m}{2}$  or  $x > \frac{m}{2}$ ),  $r = 0$ , which leads to  $\text{MD}(r) = 0$ . For the bright region of probe beam ( $-\frac{m}{2} < x < \frac{m}{2}$ ),  $r = \frac{b}{a}$ , being considerably large, which also yields  $\text{MD}(r) \approx 0$ . The situation is different, however, for the edges ( $x = -\frac{m}{2}$  or  $x = \frac{m}{2}$ ). A transition status is considered to exist, where  $I_{\text{ref}}(x) \sim I_{\text{prob}}(x)$ , making the *in situ*  $\text{MD}(r)$  maximum equal to unity [15].

In the existence of the scattering media, the scattering light field recorded by Cam<sub>1</sub> can be expressed by

$$E_{\text{out}} = TE_{\text{in}}, \quad (4)$$

where  $E_{\text{in}}$  is the light field of the probe beam before the scattering medium, and  $T$  is the transmission matrix of the scattering medium. Due to the scattering, the spatial pattern gets completely chaotic, and, as a result, the edge profile cannot be seen in the disordered optical field. Specifically, the spatial pattern evolves as a random speckle pattern when light propagates through the scattering medium in the hologram recording stage. Thus, the original spatial information is encoded in the recorded random speckle pattern; the recorded speckle pattern carries information of the original incident spatial pattern and the scattering medium. Therefore, signal input to the PCM is the fused information of  $TE_{\text{in}}$ . Due to the phase-conjugated nature, the PCM turns the input into its phase-conjugated copy,  $[TE_{\text{in}}]^*$ . In the hologram playback stage, the light field ( $E_{\text{PB}}$ ) out of the scattering medium is recorded by Cam<sub>2</sub>, which can be written as

$$E_{\text{PB}} = (T)^t [TE_{\text{in}}]^* = [(T)^+ TE_{\text{in}}]^*, \quad (5)$$

where  $*$  denotes complex conjugate while  $^t$  and  $^+$ , respectively, signify transpose and conjugate transpose.

A further justification why the time-reversal identity of DOPC is able to overcome the scattering and achieve edge enhancement simultaneously is briefed below. In the phase recording stage, Cam<sub>1</sub> records an interferogram formed by the reference beam ( $E_{\text{ref}}$ ) and the scattered probe beam ( $TE_{\text{in}}$ ). After the scattering medium, the probe beam is scrambled. In the playback section, the output light field  $[(T)^+ TE_{\text{in}}]$  from the scattering medium appears even more scrambled. But, within a time-invariant system, one can assume that  $(T)^+ T \approx I$ , where  $I$  denotes an identity matrix. That is, the output light is exactly conjugated to the probe beam. Therefore, the time-reversal playback essentially decodes the original pattern from a seemingly random speckle pattern by reciprocating the transmission matrix, enabling scattering suppression at the front side of the scattering medium.

For DOPC systems, a camera-SLM module is employed to record the probe-reference interference pattern and retrieve a phase profile to mimic the effect of grating in analogue OPC. Thus, the precision of the retrieved phase (to be loaded on the SLM) matters. In our system, the primary phase retrieval precision is determined by the smallest bit depth of the digital devices (Cam<sub>1</sub>, 16 bits; SLM, 8 bits). Through simulation (please refer to Appendix A), it is found that the calculated phase is the most accurate when the two beams of interference are equally intense, and the accuracy is reduced with increased imbalance in beam ratio (see Appendix A, Fig. 6). Therefore, in our system, when the beam ratio  $r = 1$ , the whole object can be recovered with fair fidelity due to the minimum phase error. With increased beam ratio  $r$ , for nonedge regions, the

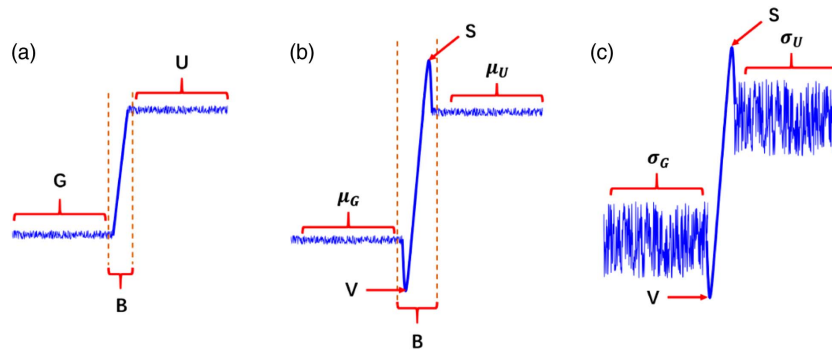


**Fig. 2.** Anatomy and metrics of an edge. (a) A regular unenhanced edge can be divided into three portions, including ground level (G), brink (B), and upper level (U). The lengths of G and U occupy 30 pixels in our experiment. (b) For an enhanced edge, the maximum and minimum pixel intensities of the portion B are termed as summit (S) and valley (V). To quantify the absolute edge enhancement effect, the concept of edge enhancement index  $EI = \frac{(S-V)/(S+V)}{(\mu_U - \mu_G)/(\mu_U + \mu_G)}$  is introduced, where  $\mu_U$  and  $\mu_G$  are mean of intensity values of U and G, respectively. (c) The noise level of an edge influences the visual enhancement effect, and thus the concept of edge ENR  $= \frac{S-V}{\sqrt{\sigma_U^2 + \sigma_G^2}}$  is defined, where  $\sigma_U$  and  $\sigma_G$  are standard deviation of the intensity values of U and G, respectively.

phase retrieval accuracy drops due to imbalance of the interfering beam ratio. But, for edges, the precision of the calculated phase remains optimum due to the existence of the transition status, where  $I_{\text{ref}}(x) \sim I_{\text{prob}}(x)$ . Under this condition ( $I_{\text{obj}} \gg I_{\text{ref}}$ ), when the SLM is illuminated by the reference beam in the playback stage, the generated conjugated light corresponding to the nonedge regions may deviate from its ideal optical paths. As a result, the nonedge regions are harder to be recovered; more and more photons contribute to the background noise when they propagate through the scattering medium. In comparison, the edge areas are reinforced from the background.

### C. Quantification of the Edge Enhancement Effect

For a characteristic unenhanced edge [Fig. 2(a)] in an intensity pattern, it can be divided into three portions, ground level (G), brink (B), and upper level (U). In our experiment, the lengths of G and U are both set to be 30 pixels. For an enhanced edge [Fig. 2(b)], two additional parameters are defined, the summit (S) (maximum pixel intensity) and the valley (V) (minimum pixel intensity) in the regime of brink. To quantify the absolute edge enhancement effect, the concept of the edge enhancement index (EI) is introduced [36,37]:  $EI = \frac{(S-V)/(S+V)}{(\mu_U - \mu_G)/(\mu_U + \mu_G)}$ , where  $\mu_U$  and  $\mu_G$  are the mean of intensity values of U and G, respectively. For a nonenhanced typical edge,  $\mu_U \approx S$ ,  $\mu_G \approx V$ , and therefore the edge  $EI \approx 1$ . A larger EI indicates a greater absolute edge enhancement effect. However, only EI is not sufficient for quantifying the visual conspicuity of the edge, as the noise level also influences the visual effect [Fig. 2(c)]. Thus, the concept of edge enhancement-to-noise ratio (ENR) is also defined to quantify the edge enhancement effect relative to the noise level [36],  $ENR = \frac{S-V}{\sqrt{\sigma_U^2 + \sigma_G^2}}$ , where  $\sigma_U$  and  $\sigma_G$  are the standard deviation of the intensity values of U and G, respectively. Less noise in U and G and greater difference in S and V will lead to a larger value of ENR, indicating better visual edge enhancement effect relative to the noise level.

## 3. RESULTS AND DISCUSSION

With a fine-tuned DOPC system, experiments are conducted to enhance the edge of an intensity pattern through strong scattering media. Transmitting through the resolution test chart, the intensity profile of the probe beam is shaped into a pattern “0”, carrying the spatial information. This original pattern of interest is recorded by Cam<sub>1</sub>, as shown in Fig. 3(a). Three horizontal dashed primitive lines with the length of 280 pixels are created in Fig. 3(a), and the line charts [Figs. 3(b)–3(d)] correspondingly show the horizontal intensity distributions along these lines. In Fig. 3, “A” and “B” denote the inner and outer rim of the pattern “0”, respectively. For edge B, the mean EI and ENR are calculated as 0.91 and 42.77, respectively. Then, a scattering 600-grit ground glass diffuser (S, Fig. 1) is positioned into the DOPC system. As shown in Fig. 3(e), the intensity profile of the probe beam captured by Cam<sub>1</sub> becomes a random speckle pattern after penetrating through the ground glass, and no edge profile can be found, indicating that the spatial information of the object has been completely disordered due to scattering. Despite that, information of the object is encoded within the speckle pattern. Therefore, the next step is to selectively retrieve the edge pattern from this scrambled light field.

To demonstrate the progressive formation of DOPC-based edge enhancement through scattering media, the intensity ratio ( $r = \bar{I}_{\text{prob}}/\bar{I}_{\text{ref}}$ ) between the probe and reference beams is carefully adjusted to be 0.02, 0.10, 1.0, 10, and 50, respectively, during the hologram writing. Note that the intensity of the probe beam/speckle pattern ( $\bar{I}_{\text{prob}}$ ) is represented by the mean value of all pixels within the region of interest (ROI), e.g., Fig. 3(e), while the intensity of the reference beam ( $\bar{I}_{\text{ref}}$ ) is characterized within the same ROI in the same manner.

The intensity patterns of the conjugated light field recorded by Cam<sub>2</sub> in the playback stage are shown in Fig. 4 (the first row). As seen, the edge information can be retrieved well from random speckle patterns through DOPC. That said, there are still quite some residual speckle grains even with the DOPC compensation. Especially in Figs. 4(a) and 4(e), speckle grains

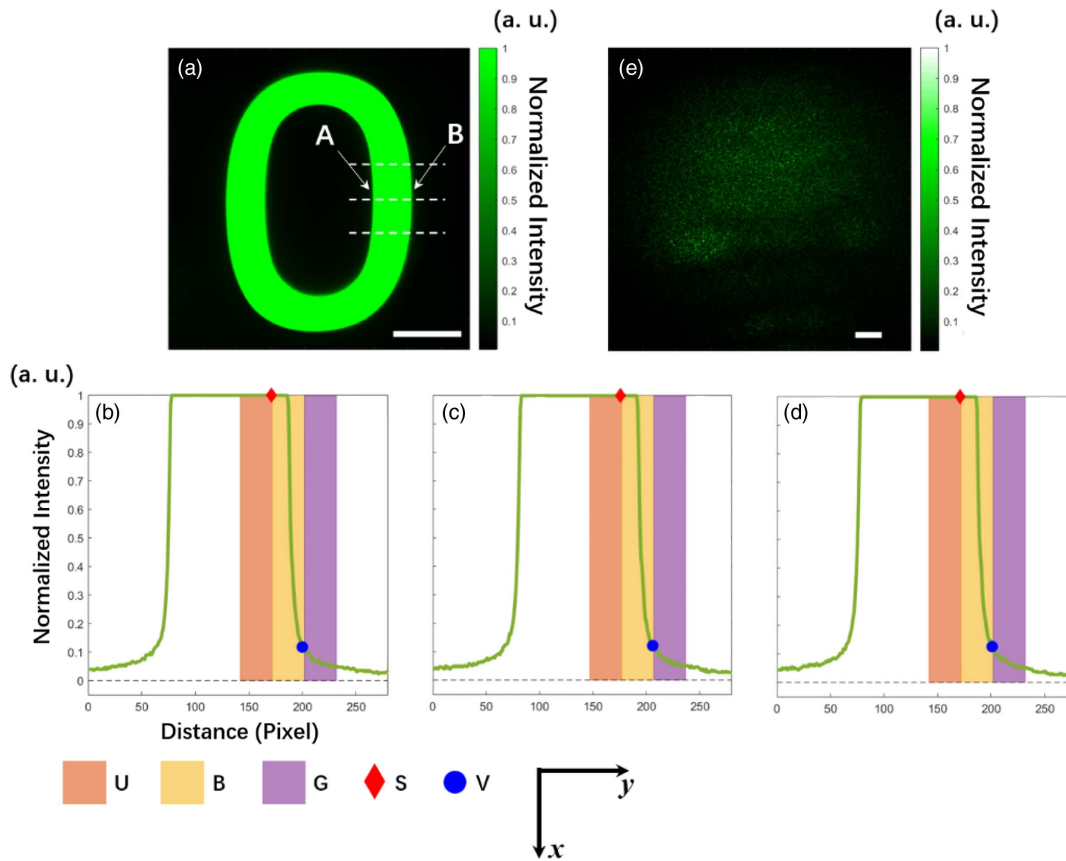


**Fig. 3.** Intensity profile of the probe beam before and after transmitting through the scattering medium. (a) Intensity profile of the incident probe beam, a quasi-binary pattern of number “0”, shaped by the resolution test chart. Three horizontal white dashed primitive lines (1–3) with the length of 280 pixels are created. The intensity distributions along the lines 1–3 are, respectively, shown in (b)–(d). A and B denote the inner and outer rim of the pattern “0”, respectively. For edge B, the mean EI and ENR are calculated as 0.91 and 42.77, correspondingly. U, upper level; B, brink; G, ground level; S, summit; V, valley. (e) Intensity profile of the probe beam after penetrating a ground glass diffuser, which is a seemingly random speckle pattern with no obvious edge profile that can be found. Scale bar, 500  $\mu\text{m}$ .

are not sufficiently suppressed because of inefficient hologram writing due to the small value of  $r$ . With increased  $r$  value, intensities of the retrieved nonedge regions are suppressed, but the edges are now selectively highlighted [Figs. 4(i), 4(m), and 4(q)]. To quantify the transition, similar to Fig. 3(a), three 280-pixel horizontal dashed lines (1–3) are created for the first row of Fig. 4. The intensity distributions along these lines are, respectively, plotted in the subfigures in the second, third, and fourth rows of Fig. 4, as indicated by the green lines. For example, Figs. 4(b)–4(d) are the intensity profiles corresponding to lines 1–3 in Fig. 4(a), while Figs. 4(f)–4(h) correspond to lines 1–3 in Fig. 4(e). As seen, when  $r$  is increased, the degree of edge enhancement is boosted due to the robust speckle elimination. When  $r = 50$ , as shown in Figs. 4(r), 4(s), and 4(t), the ratio of the noise (speckle grains) to the signal (edges) is strongly suppressed, yet the image boundaries are greatly highlighted.

It is also very important to note that while related, DOPC-based image and edge enhancement through scattering media are essentially two different directions: for regular imaging through scattering media (not aimed for edge enhancement), the optimal performance is usually acquired around  $r = 1$ ,

when the M.E. of the PCM achieves maximum at both bright region and edges (but is still zero in the dark region), as confirmed in Fig. 4(i). It should be clarified that the mean intensity of speckle in the ROI equal to that of the reference beam is not necessarily the optimal intensity ratio for recovering the full image. As seen in Fig. 4(i), edges start to protrude when  $r = 1$ . However, the situation of  $r = 1$  is the one closest to the optimal image recovery, compared to the other four intensity ratios in Fig. 4. If the purpose is to enhance the edge profile only while the other parts of the image are suppressed, a large value of  $r$  is preferred, i.e., the probe beam should be sufficiently stronger than the reference beam [as in Fig. 4(q)]. Such difference also highlights the motivation of the study as existing knowledge or experiences on optical focusing and imaging through scattering media cannot be directly applied for edge enhancement.

To further quantify the performance of DOPC-based edge enhancement through turbidity, in Fig. 5, we plot EI and ENR versus different beam intensity ratios. Each data point represents the mean value of EI or ENR from calculations of lines 1–3. The  $x$  axis represents the common logarithmic scale of the intensity ratio between the probe and reference beams,

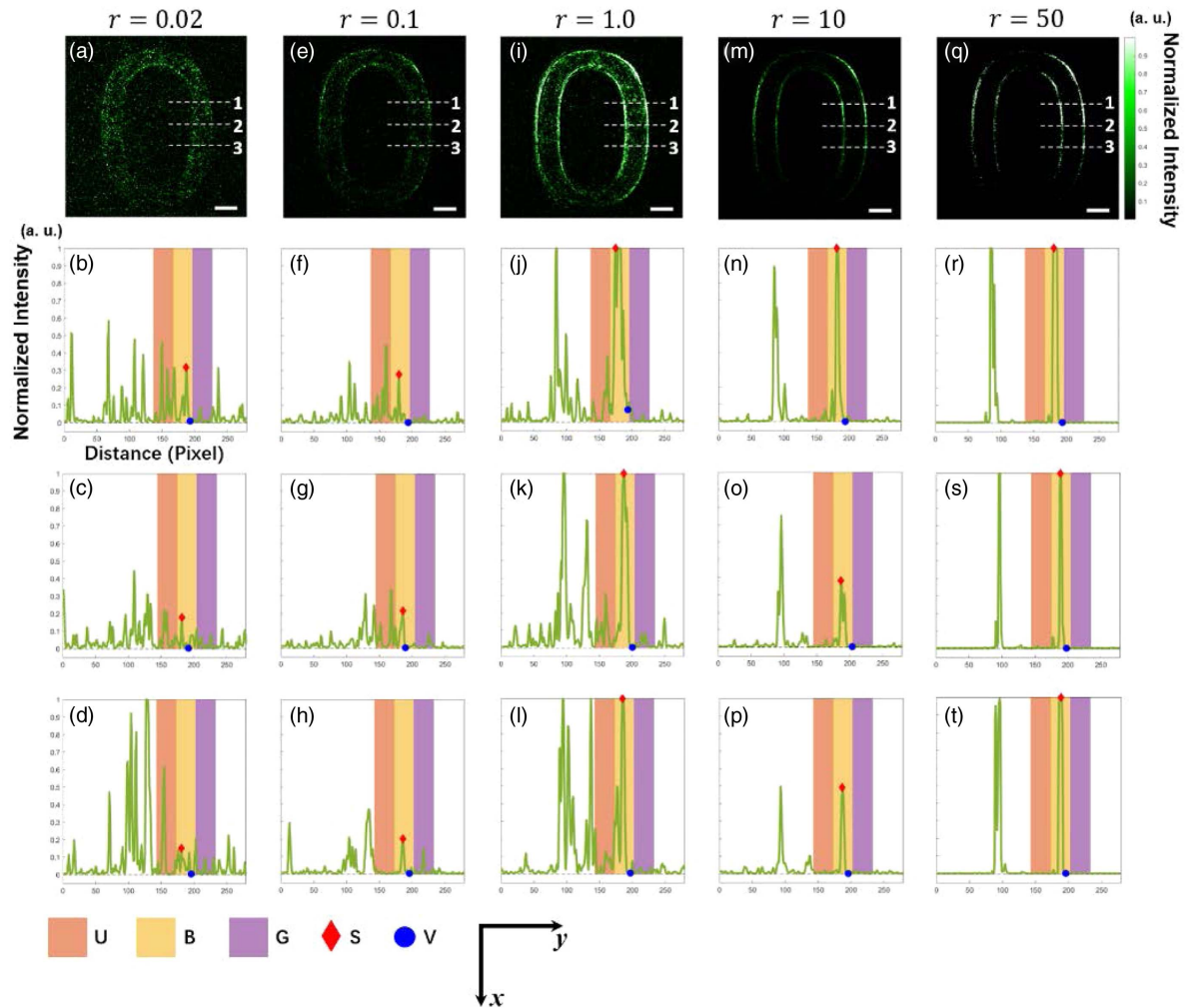


**Fig. 4.** DOPC-based edge enhancement through scattering media. Five images, (a), (e), (i), (m), (q) are recorded by the CMOS camera (Cam<sub>2</sub> in Fig. 1) in the playback stage. The intensity ratio ( $r$ ) between the probe and the reference beams is tuned to different values (0.02, 0.10, 1.0, 10, 50) during the hologram writing. Three 280-pixel horizontal dashed lines (1–3) are created for the figures in the first row. The intensity distributions along lines 1–3 are, respectively, shown in the figures in the second, third, and fourth row, as indicated by the green lines. For example, (b)–(d) are the intensity profiles corresponding to lines 1–3 in (a), while (f)–(h) correspond to the lines in (e). U, upper level; b, brink; G, ground level; S, summit; V, valley. Scale bar, 250  $\mu\text{m}$ .

i.e.,  $\lg(r)$ . As seen, the mean EI (to the left axis) increases from 2.18 ( $r = 0.02$ ) to 18.52 ( $r = 50$ ), and the mean ENR (to the right axis) increases from 2.00 ( $r = 0.02$ ) to 525.94 ( $r = 50$ ). Even compared to the direct image of the object in free space [Fig. 3(a)], whose mean EI and mean ENR are, respectively, 0.91 and 42.77, the effect of edge enhancement as measured by these two parameters is quite significant, even though a strong scattering medium is penetrated.

The aforementioned results once again confirm the rationality of the proposed method to enhance the object boundary through scattering media. Without wavefront manipulation, optical signals, which are an intensity spatial pattern in this study, are thoroughly disordered when transmitting through scattering media and become seemingly random speckle patterns. In this work, DOPC serves as an effective turbidity suppressor and is able to manipulate the optical wavefronts even

through complex media. By tuning the probe-reference beam intensity ratio and hence the local modulation efficiency of the PCM as well as calculated phase precision, DOPC is capable of generating a modulated wavefront so that the edge profile can be significantly reinforced from massive speckle noise. That said, we should note the limitation of the performance. Even with a perfect DOPC system, the recovery efficiency is still limited due to the finite control elements of the SLM and other factors such as the uneven spatial distribution of the optical beams and the system calibration imperfection. As a result, only a fraction of speckles are collected, and only a fraction of the transmission matrix of the scattering medium is utilized to time-reverse the scattered probe beam. Therefore, in practice, DOPC is not able to totally overcome scattering, and the recovered edges are still influenced by scattering, as can be observed in Fig. 4.

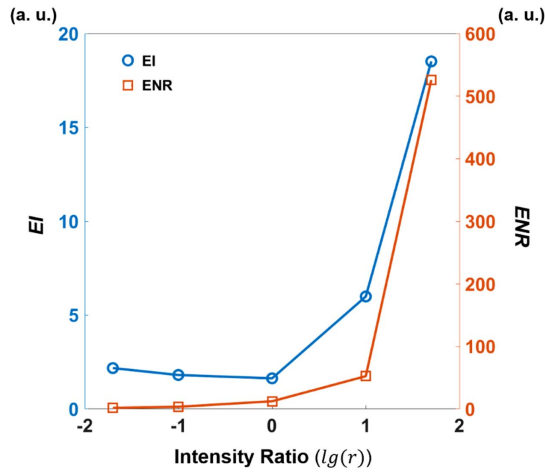


**Fig. 5.** Edge enhancement index (EI) and edge enhancement-to-noise ratio (ENR) of edge B for different values of  $r$  (0.02, 0.10, 1.0, 10, 50). The  $x$  axis represents the common logarithmic scale of the intensity ratio between the probe and reference beams, i.e.,  $\lg(r)$ . EI increases from 2.18 to 18.52, and ENR increases from 2.00 to 525.94.

#### 4. CONCLUSION

Edge enhancement plays an important role in many aspects of optical imaging and image processing. Recent developments in optical wavefront shaping have paved the way to achieve high quality optical focusing and imaging within or through scattering media; edge enhancement through strong turbidity, however, remains unexplored. While related, existing knowledge or experiences cannot be directly applied for edge enhancement through scattering media. In this study, we propose an effective two-step DOPC approach. First, a digital hologram is obtained, where information of the object and the edge is encoded with distinct accuracy (high for edges but low for nonedge regions); second, the edge profile is reinforced by phase conjugating the

scattered light while the nonedge regions are significantly suppressed. In experiment, with a 600-grit ground glass diffuser as the scattering medium, our method allowed for significant visual enhancement of the edges from noisy speckle patterns. As measured by the EI and ENR, the edges can be reinforced by  $\sim 8.5$  and  $\sim 263$  times, respectively, benefiting from the robust speckle suppression capability. To the best of our knowledge, this is the first time that edge information of a spatial pattern has been extracted clearly through strong turbidity. Moreover, the performance of the edge extraction and enhancement is controllable through tuning the efficiency of the PCM. With further development, this approach may potentially find broad applications or inspire new methods to enrich the comprehension of optical images in the scenario of scattering, such as at depths in biological tissue.

#### APPENDIX A: BEAM INTENSITY RATIO INFLUENCE ON PHASE RETRIEVAL ACCURACY

Here we discuss how the intensity ratio of two interfering optical beams affects the accuracy of retrieved phase difference between them. As shown in Fig. 6(a), green vector ( $E_0$ ) represents the electric field of one optical beam, and blue ( $E_1$ ) and red ( $E_2$ ) vectors stand for the electric field of other beams, with distinct magnitudes in two cases (equal and unequal cases). The probe beam ( $E_{\text{prob}}$ ) and reference beam ( $E_{\text{ref}}$ ) (described in the paper) can correspond to any one of these three vectors depending on their values. In the first case,  $E_1$  has the same magnitude as  $E_0$ , suggesting that the intensities of these two beams ( $I_a$  and  $I_b$ ) are the same, i.e.,  $r = \frac{I_a}{I_b} = \frac{|E_0|^2}{|E_1|^2} = 1$ ; in the second case,  $E_2$  has smaller magnitude than  $E_1$ . The resultant optical field can be obtained by vector addition. Within a given intensity resolution interval of a digital camera, all intensity values within this interval yield the same digital output at the photosensor. In other words, the digital records of interferograms that lie in a single intensity resolution interval are identical. Therefore, phase difference between two optical beams cannot be resolved,

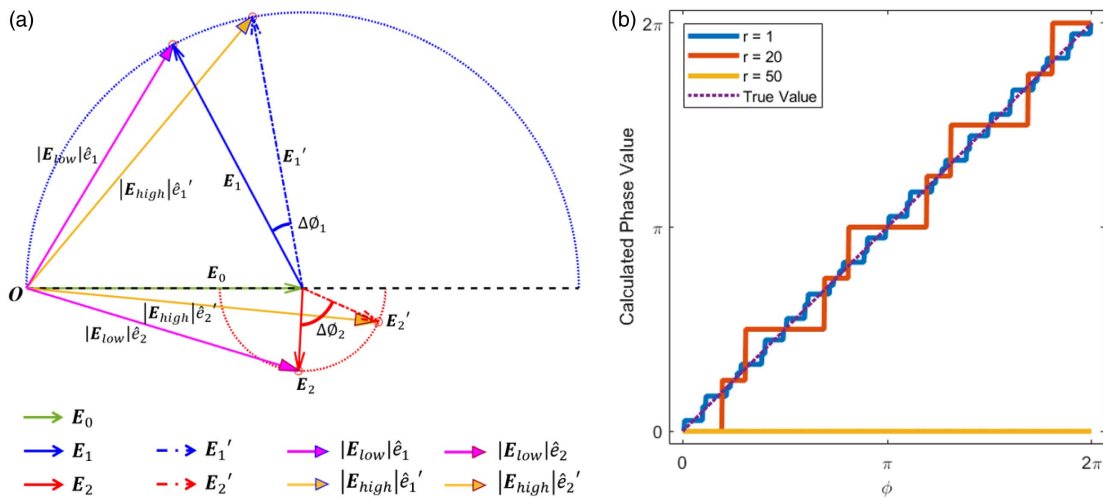


**Fig. 6.** (a) Schematic diagram illustrating how the intensity ratio between two optical beams affects the resolvability of phase by the interferogram. Different types of vectors represent the electric field of different beams, as presented by the legend.  $\Delta\phi_{1,2}$ , the smallest resolvable interval of phase. (b) Retrieved phase value by the four-step phase-shift method, under the “round-off” effect of the digital camera.  $r$  is the intensity ratio between the two optical beams that are interfering, i.e.,  $r = \frac{I_a}{I_b}$ .

unless the intensity of the interferogram differs by at least one intensity resolution interval of the camera. For a given intensity resolution interval, i.e.,  $[I_{\text{low}}, I_{\text{high}}]$ , their lower and upper intensity limits are corresponding to two electric field vectors that have small difference in magnitude, i.e.,  $E_{\text{low}}$  and  $E_{\text{high}}$ , where  $|E_{\text{low}}|^2 = 2I_{\text{low}}/c\epsilon_0$  and  $|E_{\text{high}}|^2 = 2I_{\text{high}}/c\epsilon_0$  ( $c$ , the speed of light;  $\epsilon_0$ , permittivity of free space).  $E_{\text{low}}$  and  $E_{\text{high}}$  for the above-mentioned two different cases are accordingly signified by the two pairs of magenta and yellow vectors ( $|E_{\text{low}}|\hat{e}_1$  &  $|E_{\text{high}}|\hat{e}'_1$  and  $|E_{\text{low}}|\hat{e}_2$  &  $|E_{\text{high}}|\hat{e}'_2$ , where  $\hat{e}_1$ ,  $\hat{e}'_1$ ,  $\hat{e}_2$ , and  $\hat{e}'_2$  are unit vectors). For the first case ( $r = 1$ ), i.e., the upper semicircle in Fig. 6(a),  $E'_1$  will yield the same digital record of the interferogram as  $E_1$ , since their resultant intensity values lie in a single intensity resolution interval  $[I_{\text{low}}, I_{\text{high}}]$ . Therefore, the smallest resolvable phase change (precision) by the interferogram is  $\Delta\phi_1$ . For the second case ( $r > 1$ ), i.e., the lower semicircle in Fig. 6(a),  $E'_2$  will produce the same digital record of the interferogram as  $E_2$ , being similar to the first case. As a result, the smallest resolvable phase range (precision) by the interferogram for the second case is  $\Delta\phi_2$ . As seen qualitatively,  $\Delta\phi_2 > \Delta\phi_1$ , which means the resolvability (precision) of phase change by interferogram is underoptimized when one beam is more intense than the other. Moreover, it can be inferred that when  $r \gg 1$ , i.e., one light beam is far more intensive than the other, the resolvability (precision) of the phase change by the interferogram becomes even worse.

In our experiment, a four-step phase-shift method [38] was applied to retrieve the phase difference ( $\phi$ ) between the two optical beams. The interferograms projected to  $\text{Cam}_1$  (as in Fig. 1) can be written as

$$I_{b,i} = I_{a,i} + I_{b,i} + 2 \cos(\phi + i \cdot \pi/2) \sqrt{I_{a,i} \cdot I_{b,i}}, \quad i = 0, 1, 2, 3. \quad (\text{A1})$$

However, all these four digital records of the interferogram suffer from the “round-off” effect due to the nature of digital cameras, as discussed above. When one light beam has a larger intensity than the other, the “round-off” effect compromises the fidelity of phase retrieval. The exact digital records of four interferograms, denoted by  $[I_b]_i$  ( $i = 0, 1, 2, 3$ ), are utilized to calculate phase value through

$$\phi_{\text{cal}} = \arg\{([I_b]_0 - [I_b]_2) + j \cdot ([I_b]_1 - [I_b]_3)\}, \quad (\text{A2})$$

where  $\arg\{\}$  denotes taking the phase angle of a complex number. Based on Eqs. (A1) and (A2), the phase retrieval by the four-step phase-shift approach under the “round-off” effect is simulated, as shown in Fig. 6(b). As seen,  $r = 1$  gives the best approximation to the true value; when  $r$  increases, however, the calculated phase values deviate more from the true curve. The phase value even cannot be retrieved when  $r$  approaches a large value, say  $r = 50$ , which may lead to a completely invalid measurement over the entire range of phase ( $0$  to  $2\pi$ ).

In brief summary, the retrieved phase profile is most accurate when the two beams of interference are equally intense *in situ*, and the accuracy is reduced with increased imbalance in the beam ratio.

**Funding.** National Natural Science Foundation of China (81627805, 81671726, 81671851, 81827808, 81930048); National Key Research and Development Program of China (2016YFC0103803, 2017YFA0700401); Hong Kong Research Grants Council, University Grants Committee (25204416); Hong Kong Innovation and Technology Commission (ITS/022/18); Shenzhen Science and Technology Innovation Commission (JCYJ20170818104421564); CAS Scientific Instrument RD Programs (YJKYYQ20170075).

**Disclosures.** The authors declare no conflicts of interest.

<sup>†</sup>These authors contributed equally to this work.

## REFERENCES

1. H. Ge, B. Wang, W. Ji, J. Wei, L. Wang, and Z. Huang, “Photorefractive edge-enhancement and its application to pattern recognition,” *Proc. SPIE* **5280**, 777–784 (2004).
2. A. Jesacher, S. Furrer, S. Bernet, and M. Ritsch-Marte, “Shadow effects in spiral phase contrast microscopy,” *Phys. Rev. Lett.* **94**, 233902 (2005).
3. P. Nisthula and R. Yadhu, “A novel method to detect bone cancer using image fusion and edge detection,” *Int. J. Eng. Comp. Sci.* **2**, 2012–2018 (2013).
4. F. Qadir, M. Peer, and K. Khan, “Efficient edge detection methods for diagnosis of lung cancer based on two-dimensional cellular automata,” *Adv. Appl. Sci. Res.* **3**, 2050–2058 (2012).
5. M. Divakar, P. K. Patel, and K. Gupta, “Cellular automata based edge-detection for brain tumor,” in *International Conference on Advances in Computing, Communications and Informatics* (IEEE, 2013), pp. 53–59.
6. D. Lu, X.-H. Yu, X. Jin, B. Li, Q. Chen, and J. Zhu, “Neural network based edge detection for automated medical diagnosis,” in *IEEE International Conference on Information and Automation* (IEEE, 2011), pp. 343–348.
7. F. Zernike, “Phase contrast, a new method for the microscopic observation of transparent objects,” *Physica* **9**, 686–698 (1942).
8. T. Zhu, Y. Zhou, Y. Lou, H. Ye, M. Qiu, Z. Ruan, and S. Fan, “Plasmonic computing of spatial differentiation,” *Nat. Commun.* **8**, 15391 (2017).
9. A. Grossmann, “Wavelet transforms and edge detection,” in *Stochastic Processes in Physics and Engineering*, S. Albeverio, P. Blanchard, M. Hazewinkel, and L. Streit, eds. (Springer, 1988), pp. 149–157.
10. K. Kohlmann, “Corner detection in natural images based on the 2-D Hilbert transform,” *Sig. Process.* **48**, 225–234 (1996).
11. M. Ritsch-Marte, “Orbital angular momentum light in microscopy,” *Phil. Trans. R. Soc. A* **375**, 20150437 (2017).
12. X. D. Qiu, F. S. Li, W. H. Zhang, Z. H. Zhu, and L. X. Chen, “Spiral phase contrast imaging in nonlinear optics: seeing phase objects using invisible illumination,” *Optica* **5**, 208–212 (2018).
13. S.-K. Liu, C. Yang, S.-L. Liu, Z.-Y. Zhou, Y. Li, Y.-H. Li, Z.-H. Xu, G.-C. Guo, and B.-S. Shi, “Up-conversion imaging processing with field-of-view and edge enhancement,” *Phys. Rev. Appl.* **11**, 044013 (2019).
14. S. Furrer, A. Jesacher, S. Bernet, and M. Ritsch-Marte, “Spiral phase contrast imaging in microscopy,” *Opt. Express* **13**, 689–694 (2005).
15. J. Feinberg, “Real-time edge enhancement using the photorefractive effect,” *Opt. Lett.* **5**, 330–332 (1980).
16. J. Huignard and J. Herriau, “Real-time coherent object edge reconstruction with  $\text{Bi}_{12}\text{SiO}_{20}$  crystals,” *Appl. Opt.* **17**, 2671–2672 (1978).
17. J. O. White and A. Yariv, “Real-time image processing via four-wave mixing in a photorefractive medium,” in *Landmark Papers on Photorefractive Nonlinear Optics* (World Scientific, 1995), pp. 455–457.

18. C.-S. Guo, Y.-J. Han, J.-B. Xu, and J. Ding, "Radial Hilbert transform with Laguerre–Gaussian spatial filters," *Opt. Lett.* **31**, 1394–1396 (2006).
19. Y. Zhou, S. Feng, S. Nie, J. Ma, and C. Yuan, "Image edge enhancement using Airy spiral phase filter," *Opt. Express* **24**, 25258–25268 (2016).
20. L. V. Wang and H.-I. Wu, *Biomedical Optics: Principles and Imaging* (Wiley, 2012).
21. J. W. Goodman, *Speckle Phenomena in Optics: Theory and Applications* (Roberts & Company, 2007).
22. Z. Ding, H. Ren, Y. Zhao, J. S. Nelson, and Z. Chen, "High-resolution optical coherence tomography over a large depth range with an axicon lens," *Opt. Lett.* **27**, 243–245 (2002).
23. P. Lai, X. Xu, H. Liu, Y. Suzuki, and L. V. Wang, "Reflection-mode time-reversed ultrasonically encoded optical focusing into turbid media," *J. Biomed. Opt.* **16**, 080505 (2011).
24. Y. Liu, P. Lai, C. Ma, X. Xu, A. A. Grabar, and L. V. Wang, "Optical focusing deep inside dynamic scattering media with near-infrared time-reversed ultrasonically encoded (TRUE) light," *Nat. Commun.* **6**, 5904 (2015).
25. C. Ma, F. Zhou, Y. Liu, and L. V. Wang, "Single-exposure optical focusing inside scattering media using binarized time-reversed adapted perturbation," *Optica* **2**, 869–876 (2015).
26. I. M. Vellekoop and A. Mosk, "Focusing coherent light through opaque strongly scattering media," *Opt. Lett.* **32**, 2309–2311 (2007).
27. Z. Yaquob, D. Psaltis, M. S. Feld, and C. Yang, "Optical phase conjugation for turbidity suppression in biological samples," *Nat. Photonics* **2**, 110–115 (2008).
28. I. M. Vellekoop, M. Cui, and C. Yang, "Digital optical phase conjugation of fluorescence in turbid tissue," *Appl. Phys. Lett.* **101**, 081108 (2012).
29. K. Si, R. Fiolka, and M. Cui, "Fluorescence imaging beyond the ballistic regime by ultrasound-pulse-guided digital phase conjugation," *Nat. Photonics* **6**, 657–661 (2012).
30. J.-H. Park, Z. Yu, K. Lee, P. Lai, and Y. Park, "Perspective: wavefront shaping techniques for controlling multiple light scattering in biological tissues: toward *in vivo* applications," *APL Photon.* **3**, 100901 (2018).
31. H. Liu, X. Xu, P. Lai, and L. V. Wang, "Time-reversed ultrasonically encoded optical focusing into tissue-mimicking media with thickness up to 70 mean free paths," *J. Biomed. Opt.* **16**, 086009 (2011).
32. Z. Yu, M. Xia, H. Li, T. Zhong, F. Zhao, H. Deng, Z. Li, D. Li, D. Wang, and P. Lai, "Implementation of digital optical phase conjugation with embedded calibration and phase rectification," *Sci. Rep.* **9**, 1537 (2019).
33. Z. Yu, J. Huangfu, F. Zhao, M. Xia, X. Wu, X. Niu, D. Li, P. Lai, and D. Wang, "Time-reversed magnetically controlled perturbation (TRMCP) optical focusing inside scattering media," *Sci. Rep.* **8**, 2927 (2018).
34. Y. Liu, C. Ma, Y. Shen, J. Shi, and L. V. Wang, "Focusing light inside dynamic scattering media with millisecond digital optical phase conjugation," *Optica* **4**, 280–288 (2017).
35. D. Wang, E. H. Zhou, J. Brake, H. Ruan, M. Jang, and C. Yang, "Focusing through dynamic tissue with millisecond digital optical phase conjugation," *Optica* **2**, 728–735 (2015).
36. E. F. Donnelly, R. R. Price, and D. R. Pickens, "Quantification of the effect of system and object parameters on edge enhancement in phase-contrast radiography," *Med. Phys.* **30**, 2888–2896 (2003).
37. E. F. Donnelly and R. R. Price, "Quantification of the effect of kVp on edge-enhancement index in phase-contrast radiography," *Med. Phys.* **29**, 999–1002 (2002).
38. C. Ma, X. Xu, Y. Liu, and L. V. Wang, "Time-reversed adapted-perturbation (TRAP) optical focusing onto dynamic objects inside scattering media," *Nat. Photonics* **8**, 931–936 (2014).